PSWF-Radon approach to reconstruction from band-limited Hankel transform

Fedor Goncharov, Mikhail Isaev, Roman Novikov, Rodion Zaytsev

PSWF-Radon approach to reconstruction from band-limited Hankel transform

Fedor Goncharov
Université Paris-Saclay
CEA, List, F-91120
Palaiseau, France
fedor.goncharov@cea.fr

Mikhail Isaev
School of Mathematics and Statistics
UNSW Sydney
Sydney, NSW, Australia
isaev.m.i@gmail.com

Roman G. Novikov
CMAP, CNRS, Ecole polytechnique
Institut Polytechnique de Paris
Palaiseau, France
novikov@cmap.polytechnique.fr

Rodion Zaytsev
Faculty of Mathematics, HSE University
Igor Krichever Center for Advanced Studies
Skolkovo Institute of Science and Technology
Moscow, Russia
rvzaytsev@edu.hse.ru

Abstract

We give new formulas for reconstructions from band-limited Hankel transform of integer or half-integer order. Our formulas rely on the PSWF-Radon approach to super-resolution in multidimensional Fourier analysis. This approach consists of combining the theory of classical one-dimensional prolate spheroidal wave functions with the Radon transform theory. We also use the relation between Fourier and Hankel transforms and Cormack-type inversion of the Radon transform. Finally, we investigate numerically the capabilities of our approach to super-resolution for band-limited Hankel inversion in relation to varying levels of noise.

Keywords: Hankel transform, Fourier transform, Radon transform, prolate spheroidal wave functions, super-resolution
AMS subject classification: 42A38, 49K40, 33E10

1 Introduction

The Hankel transform of order ν is formally defined by

$$\mathcal{H}_\nu[f](t) := \int_0^\infty f(s) J_\nu(ts) \sqrt{ts}\, ds, \qquad t \in \mathbb{R}_+, \tag{1.1}$$

where J_ν is the Bessel function of the first kind and $\mathbb{R}_+ := \{\rho \in \mathbb{R} \,:\, \rho \geqslant 0\}$. If $\nu \geqslant -\frac{1}{2}$ then $\mathcal{H}_\nu$ is an invertable operator on $\mathcal{L}^2(\mathbb{R}_+)$ and $\mathcal{H}_\nu^{-1} = \mathcal{H}_\nu$, that is, the operator defined by (1.1) coincides with its own inverse.

We consider the following inverse problem.

Problem 1.1. Let $\sigma, r > 0$ and $\nu \geqslant -\frac{1}{2}$ be given. Find $f \in \mathcal{L}^2(\mathbb{R}_+)$ from $h = \mathcal{H}_\nu[f]$ given on $[0, r]$ (possibly with some noise), under a priori assumption that $\operatorname{supp} f \subseteq [0, \sigma]$.

Problem 1.1 is uniquely solvable for the noiseless case in view of the analyticity of $\mathcal{H}_\nu[f]$ on $(0, +\infty)$ under our assumptions. On the other hand, this problem is severely ill-posed in the sense of Hadamard in view of the super-exponential decay of the eigenvalues of the band-limited Hankel transform; see [20, Lemma 1]. For introduction into the theory of ill-posed problems; see, for example, [11, 33].

In the present work, we consider Problem 1.1 with integer or half-integer order $\nu \geqslant 0$ in connection with the problem of reconstructing unknown function supported in the ball $B_\sigma \subset \mathbb{R}^d$, $d \geqslant 2$, from its Fourier transform given on the ball B_r under a priori assumptions of the cylindrical or spherical symmetry, and also for more general cases of variable separation in polar coordinates. Here, for $\rho \in \mathbb{R}_+$, we let

$$B_\rho := \{q \in \mathbb{R}^d \,:\, |q| \leqslant \rho\}.$$

Applications of Problem 1.1 include multidimensional monochromatic inverse scattering in the Born approximation and inverse source problems; see [3,14,16,24,27] and references therein. See also [20,21] for other important applications. For information on the problem of band-limited Fourier inversion without a priori assumptions of spherical-type symmetry, including various results and approaches; see, for example, [2–4, 7, 9, 13–17, 22, 24, 28].

A possible approach for solving Problem 1.1 is based on the following approximation

$$f \approx f_{\text{naive}} := \mathcal{H}_\nu^{-1}\left[h^{\text{ext}}\right] \text{ on } [0, \sigma], \tag{1.2}$$

where

$$h^{\text{ext}}(t) := \begin{cases} h(t), & \text{for } t \in [0, r], \\ 0, & \text{otherwise.} \end{cases}$$

Formula (1.2) leads to a stable and accurate reconstruction for sufficiently large r. However, similarly to the reconstruction from the Fourier transform given on the ball B_r, this naive approach has the *diffraction limit*: small details (especially less than π/r) are blurred. The term *super-resolution* refers to the techniques that allow reconstruction beyond this diffraction limit.

In the present work we give new theoretical and numerical results for Problem 1.1 with integer or half-integer $\nu \geqslant 0$ following the PSWF-Radon approach of [15–17] to Fourier analysis in dimension $d = 2, 3$. In connection with the PSWF theory, we consider the integral operator $\mathcal{F}_c$ on $\mathcal{L}^2([-1,1])$, defined by

$$\mathcal{F}_c[f](x) := \int_{-1}^{1} e^{icxy} f(y) dy, \tag{1.3}$$

where $c > 0$ is the *bandwidth parameter*. The eigenfunctions $(\psi_{j,c})_{j\in\mathbb{N}}$ of $\mathcal{F}_c$ are *prolate spheroidal wave functions* (PSWFs), where $\mathbb{N} := \{0, 1 \ldots\}$. Recall that the operator $\mathcal{F}_c$ and its inverse admit the singular value decompositions:

$$\mathcal{F}_c[f](x) = \sum_{j\in\mathbb{N}} \mu_{j,c}\psi_{j,c}(x) \int_{-1}^{1} \psi_{j,c}(y) f(y) dy, \tag{1.4}$$

$$\mathcal{F}_c^{-1}[g](y) = \sum_{j\in\mathbb{N}} \frac{1}{\mu_{j,c}}\psi_{j,c}(y) \int_{-1}^{1} \psi_{j,c}(x) g(x) dx. \tag{1.5}$$

In addition, we can assume that $0 < |\mu_{j+1,c}| < |\mu_{j,c}|$ for all $j \in \mathbb{N}$. For more details on the PSWF theory, see [1, 5, 6, 15, 18, 31, 34, 35].

First, we consider the case of integer ν.

Theorem 1.1. *Let $\nu \in \mathbb{N}$, $r, \sigma > 0$, and $c := r\sigma$. Let $f \in \mathcal{L}^2(\mathbb{R}_+)$ be supported in $[0, \sigma]$. Then, transform $h := \mathcal{H}_\nu[f]$ on $[0, r]$ uniquely determines f by the formula*

$$f(s) = -\frac{2i^\nu}{\sigma}\sqrt{s}\frac{d}{ds}\int_s^\sigma \frac{s\,T_\nu(t/s)}{t(t^2 - s^2)^{\frac{1}{2}}}\mathcal{F}_c^{-1}[h_{r,\nu}](t/\sigma)dt, \qquad s \in (0, \sigma], \tag{1.6}$$

where T_ν is the Chebyshev polynomial of the first kind of order ν and

$$h_{r,\nu}(x) := \begin{cases} \frac{1}{\sqrt{rx}}h(rx), & \text{if } x \in [0, 1], \\ (-1)^\nu \frac{1}{\sqrt{-rx}}h(-rx), & \text{if } x \in [-1, 0). \end{cases} \tag{1.7}$$

Second, we consider the case of half-integer ν.

Theorem 1.2. *Let $n := \nu - \frac{1}{2} \in \mathbb{N}$, $r, \sigma > 0$, and $c := r\sigma$. Let $f \in \mathcal{L}^2(\mathbb{R}_+)$ be supported in $[0, \sigma]$. Then, $h := \mathcal{H}_\nu[f]$ on $[0, r]$ uniquely determines f by the formula*

$$f(s) = \frac{\sqrt{2\pi}\, i^n}{\sigma} s \frac{d^2}{ds^2} \int_s^\sigma \frac{sP_n(t/s)}{t^2} \mathcal{F}_c^{-1}[h_{r,\nu}](t/\sigma)dt, \qquad s \in (0, \sigma], \tag{1.8}$$

where P_n is the Legendre polynomial of order n and

$$h_{r,\nu}(x) := \begin{cases} \frac{1}{rx} h(rx), & \text{if } x \in [0, 1], \\ (-1)^n \frac{1}{rx} h(-rx), & \text{if } x \in [-1, 0). \end{cases} \tag{1.9}$$

Note that the function $h_{r,\nu}$ considered in (1.7) and (1.9) has no singularity at 0 under our assumptions, in view of the definition of the Hankel transform in (1.1).

We prove Theorem 1.1 and Theorem 1.2 in Section 2 using the PSWF-Radon approach for reconstruction from the band-limited Fourier transform developed in [15–17], classical formulas relating the Fourier and Hankel transforms, and Cormack-type formulas for inversion of the Radon transform. It is known that Cormack's formulas have good numerical properties for small ν but instability increases exponentially as ν grows; see, for example, [25, Section II.2]. A more stable approach relies on the *filtered back projection* (FBP) algorithm which can be derived from the classical Radon inversion formula; see [25,29] for more details in the case of $d = 2$ (and the same ideas would work for $d = 3$). Therefore, we employ FBP-based algorithms for our numerical implementation of band-limited Hankel transform inversion; see Section 3 for detailed presentation.

Figure 1.1 and Figure 1.2 illustrate our numerical reconstruction for Problem 1.1, where $\nu = 0$ and $\nu = 0.5$, respectively, and $\sigma = 1$, $r = 10$. Here, we use two-dimensional visialisation of our results in the form $v(x) = f(|x|)$, where $x \in \mathbb{R}^d$ for $d = 2$ and for $d = 3$ (displaying central cross section), for the preimage, its naive reconstruction based on (1.2), and its PSWF-Radon reconstruction with an appropriate regularisation. In particular, this also illustrates reconstruction of v from its band-limited Fourier transform under additional a priori assumption of spherical symmetry (in view of classical relation between the Fourier and Hankel transforms). The preimage considered in Figures 1.1 and 1.2 is the characteristic function of $[0.15, 0.3] \cup [0.5, 0.75]$. Note that the gaps and the internal ring width are essentially smaller that the diffraction limit $\pi/10 \approx 0.31$; therefore, the standard naive approach via (1.2) is incapable to distinguish these details. In contrast, the PSWF-Radon approach succeeds to recover preimage for both $\nu = 0$ and $\nu = 0.5$. Furthermore, for this preimage, our super-resolution reconstruction remain adequate even in the presence of moderate noise of 10% for $\nu = 0$ and 5% for $\nu = 0.5$; see

Section 3 for more detailed investigation on the stability of the PSWF-Radon approach to the band-limited Hankel transform inversion.

In Section 4, we provide additional discussion on the PSWF-Radon approach, comparing it with other possible approaches to Problem 1.1 and outlining future directions for development.

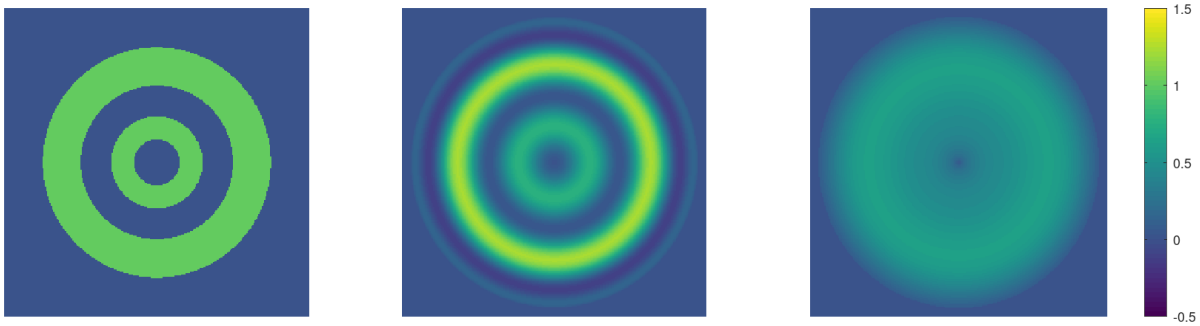

(a) **(b)** **(c)**

Figure 1.1: An example of reconstruction for Problem 1.1 with $\nu = 0$, $\sigma = 1$, $r = 10$: (a) preimage, (b) PSWF-Radon reconstruction, (c) reconstructio via (1.2).

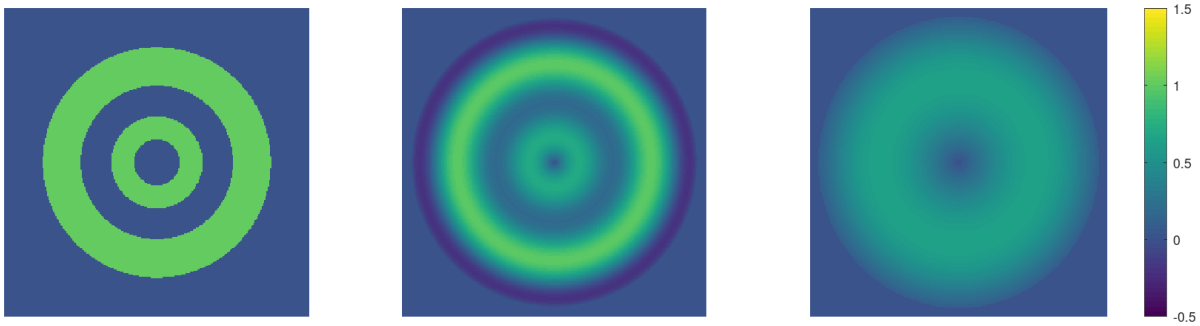

(a) **(b)** **(c)**

Figure 1.2: An example of reconstruction for Problem 1.1 with $\nu = 0.5$, $\sigma = 1$, $r = 10$: (a) preimage, (b) PSWF-Radon reconstruction, (c) reconstruction via (1.2).

2 Proofs of the theorems

We consider the classical Fourier transform $\mathcal{F}$ defined by

$$\mathcal{F}[v](p) := \frac{1}{(2\pi)^d} \int_{\mathbb{R}^d} e^{ipq} v(q) dq, \qquad p \in \mathbb{R}^d. \tag{2.1}$$

First, we recall the formulas from [15] for reconstruction v from $\mathcal{F}[v]$ limited to the ball B_r for a compactly supported v. Then, we prove Theorem 1.1 and Theorem 1.2.

Theorem 2.1 (Isaev, Novikov [15]). *Let $d \geqslant 1$, $r, \sigma > 0$ and $c = r\sigma$. Let $v \in \mathcal{L}^2(\mathbb{R}^d)$ and $\operatorname{supp} v \subset B_\sigma$. Then, its Fourier transform $\mathcal{F}[v]$ restricted to B_r determines v via the following formulas:*

$$\begin{aligned}
v(q) &= \mathcal{R}^{-1}[w_{r,\sigma}](\sigma^{-1} q), \qquad q \in \mathbb{R}^d, \\
w_{r,\sigma}(y,\theta) &= \begin{cases} \mathcal{F}_c^{-1}[g_{r,\theta}](y), & \text{if } y \in [-1,1] \\ 0, & \text{otherwise,} \end{cases} \\
g_{r,\theta}(x) &= \left(\frac{2\pi}{\sigma}\right)^d \mathcal{F}[v](rx\theta), \qquad x \in [-1,1],\ \theta \in \mathbb{S}^{d-1},
\end{aligned}$$

where $\mathcal{F}_c^{-1}$ is defined by (1.5) and $\mathcal{R}^{-1}$ is the inverse Radon transform.

In the above theorem, $\mathcal{R}$ is the classical Radon transform defined by

$$\mathcal{R}_\theta[v](y) = w(y,\theta) := \int_{q \in \mathbb{R}^d \,:\, q\theta = y} v(q) dq, \qquad y \in \mathbb{R},\ \theta \in \mathbb{S}^{d-1}.$$

There are multiple ways to compute $\mathcal{R}^{-1}$; see, for example, [25]. We use Cormack-type formulas assuming that v is compactly supported. For $d = 2$ and $q \neq 0$, we have

$$\begin{aligned}
v(q) &= \mathcal{R}^{-1}[w] = \sum_{n=-\infty}^{+\infty} v_n(|q|) e^{in\phi}, \qquad \frac{q}{|q|} = (\cos\phi, \sin\phi) \\
v_n(s) &= -\frac{1}{\pi} \frac{d}{ds} \int_s^{+\infty} \frac{s T_{|n|}(t/s) w_n(t)}{t\sqrt{t^2 - s^2}} dt, \qquad s > 0,
\end{aligned} \tag{2.2}$$

where $T_{|n|}$ is the Chebyshev polynomial of the first kind and $(w_n)_{n \in \mathbb{Z}}$ are defined by

$$w(t,\theta) = \sum_{n=-\infty}^{+\infty} w_n(t) e^{in\psi}, \qquad t > 0,\ \theta = (\cos\psi, \sin\psi).$$

For $d = 3$ and $q \neq 0$, we have

$$\begin{aligned}
v(q) &= \mathcal{R}^{-1}[w] = \sum_{n=0}^{+\infty} \sum_{k=-n}^{n} v_{n,k}(|q|)\, Y_{n,k}\left(\frac{q}{|q|}\right), \\
v_{n,k}(s) &= \frac{1}{2\pi} \cdot \frac{d^2}{ds^2} \int_s^{+\infty} \frac{s P_n(t/s)}{t^2} w_{n,k}(t) dt, \qquad s > 0,
\end{aligned} \tag{2.3}$$

where $Y_n^k : \mathbb{S}^2 \to \mathbb{R}$ is the spherical harmonic for each $n \in \mathbb{N}$ and $|k| \leqslant n$, P_n is the Legendre polynomial, and $(w_n^k)_{n\in\mathbb{N},|k|\leqslant n}$ are defined by

$$w(t,\theta) = \sum_{n=0}^{+\infty} \sum_{k=-n}^{n} w_{n,k}(t) Y_{n,k}(\theta), \qquad t > 0,\ \theta \in \mathbb{S}^2.$$

Remark 2.2. Note that formula (2.3) is usually stated in an alternative form with

$$v_{n,k}(s) = \frac{1}{2\pi s} \int_s^{+\infty} P_n(t/s) w''_{n,k}(t) dt, \qquad s > 0.$$

where $w''_{n,k}$ is the second derivative of $w_{n,k}$; see, for example, [25, Theorem 2.3]. If v is sufficiently smooth and compactly supported (implying that $w_{n,k}$ is such as well), one can show the equivalence by using the following formula twice:

$$\int_s^{+\infty} F(t/s) G'(t) dt = s \frac{d}{ds} \left(\frac{1}{s} \int_s^{+\infty} \tilde{F}(t/s) G(t) dt \right), \qquad \tilde{F}(t/s) := \frac{t}{s} F(t/s),$$

where F, G are smooth on $(0, +\infty)$ and G is compactly supported. This also extends to non-smooth v, but we prefer the form of (2.3) as it does not require consideration of generalised derivatives.

2.1 Proof of Theorem 1.1

For non-zero $q \in \mathbb{R}^2$, we introduce the notation $\varphi_q \in [0, 2\pi)$ defined by

$$\frac{q}{|q|} = (\cos \varphi_q, \sin \varphi_q).$$

Recall that if $v \in \mathcal{L}^2(\mathbb{R}^2)$ is expanded in the series

$$v(q) = \sum_{n=-\infty}^{+\infty} v_n(|q|) e^{in\varphi_q},$$

then its Fourier transform (2.1) satisfies

$$\mathcal{F}[v](p) = \frac{1}{2\pi\sqrt{|p|}} \sum_{n=-\infty}^{+\infty} i^n \mathcal{H}_n[f_n](|p|) e^{in\varphi_p}, \tag{2.4}$$

where $p \in \mathbb{R}^2$ is non-zero and

$$f_n(s) := v_n(s) \cdot \sqrt{s}, \qquad s \in \mathbb{R}_+.$$

To prove Theorem 1.1, we apply Theorem 2.1 to the function v defined by

$$v(q) := \frac{f(|q|)}{\sqrt{|q|}} e^{i\nu\varphi_q}.$$

Since, by our assumptions, $f \in \mathcal{L}^2(\mathbb{R}_+)$, we get that $v \in \mathcal{L}^2(\mathbb{R}^2)$. Using (2.4), we get that

$$\mathcal{F}[v](p) = \frac{i^\nu}{2\pi\sqrt{|p|}} \mathcal{H}_\nu[f](|p|) e^{i\nu\varphi_p}.$$

Taking $p = rx\theta$ and recalling $h_{r,\nu}$ defined in (1.7), we find that

$$g_{r,\theta}(x) := \left(\frac{2\pi}{\sigma}\right)^2 \mathcal{F}[v](rx\theta) = \frac{2\pi i^\nu}{\sigma^2} h_{r,\nu}(x) e^{i\nu\varphi}, \qquad x \in [-1,1]. \tag{2.5}$$

where $\theta = (\cos\varphi, \sin\varphi)$. Next, we observe that

$$w_{r,\sigma}(y,\theta) := \mathcal{F}_c^{-1}[g_{r,\theta}](y) = \frac{2\pi i^\nu e^{i\nu\varphi}}{\sigma^2} \mathcal{F}_c^{-1}[h_{r,\nu}](y), \qquad y \in [-1,1].$$

Applying Theorem 2.1 and Cormack's formula (2.2), we find that

$$\begin{aligned} v(\sigma x\theta) &= \mathcal{R}^{-1}[w_{r,\sigma}](x) \\ &= -\frac{e^{i\nu\varphi}}{\pi} \frac{d}{dx} \int_x^{+\infty} \frac{x T_\nu(y/x) w_\nu(y)}{y\sqrt{y^2 - x^2}} dy, \qquad x \in (0,1], \end{aligned}$$

where

$$w_\nu(y) := \begin{cases} \frac{2\pi i^\nu}{\sigma^2} \mathcal{F}_c^{-1}[h_{r,\nu}](y), & \text{if } y \in (0,1], \\ 0, & \text{if } y > 1. \end{cases}$$

Substituting $s = \sigma x$, $t = \sigma y$, and recalling the definition of v, we derive formula (1.6). This completes the proof of Theorem 1.1.

2.2 Proof of Theorem 1.2

The proof follows the same steps as in the previous section. First, we recall that if $v \in \mathcal{L}^2(\mathbb{R}^3)$ is expanded in the series

$$v(q) = \sum_{n=0}^{+\infty} \sum_{k=-n}^{n} v_{n,k}(|q|)\, Y_{n,k}\left(\frac{q}{|q|}\right),$$

then its Fourier transform (2.1) satisfies

$$\mathcal{F}[v](p) = \frac{1}{(2\pi)^{3/2}|p|} \sum_{n=0}^{+\infty} \sum_{k=-n}^{n} i^n \mathcal{H}_{n+\frac{1}{2}}[f_{n,k}](|p|) Y_{n,k}\left(\frac{p}{|p|}\right), \tag{2.6}$$

where $p \in \mathbb{R}^3$ is non-zero and

$$f_{n,k}(s) := v_{n,k}(s) \cdot s, \qquad s \in \mathbb{R}_+.$$

To prove Theorem 1.2, we apply Theorem 2.1 to the function v defined by

$$v(q) := \frac{f(|q|)}{|q|} Y_{n,0}\left(\tfrac{q}{|q|}\right).$$

Since, by our assumptions, $f \in \mathcal{L}^2(\mathbb{R}_+)$, we get that $v \in \mathcal{L}^2(\mathbb{R}^3)$. Using (2.6), we get that

$$\mathcal{F}[v](p) = \frac{i^n}{(2\pi)^{3/2}|p|} \mathcal{H}_\nu[f](|p|) Y_{n,0}\left(\tfrac{p}{|p|}\right).$$

Taking $p = rx\theta$ and recalling $h_{r,\nu}$ defined in (1.9), we find that

$$\begin{aligned} g_{r,\theta}(x) :&= \left(\frac{2\pi}{\sigma}\right)^3 \mathcal{F}[v](rx\theta) \\ &= \frac{(2\pi)^{3/2} i^n}{\sigma^3} h_{r,\nu}(|x|) Y_{n,0}\left(\operatorname{sgn}(x)\theta\right), \quad x \in [-1,1], \quad \theta \in \mathbb{S}^2. \end{aligned}$$

Recall that the spherical harmonic $Y_{n,k}$ with $k = 0$ can be expressed in terms of the Legendre polynomial P_n and, in particular, $Y_{n,0}(-\theta) = (-1)^n Y_{n,0}(\theta)$. Therefore, we get

$$g_{r,\theta}(x) = \frac{(2\pi)^{3/2} i^n}{\sigma^3} h_{r,\nu}(x) Y_{n,0}(\theta) \tag{2.7}$$

for all non-zero $x \in [-1,1]$. Next, we observe that

$$w_{r,\sigma}(y,\theta) := \mathcal{F}_c^{-1}[g_{r,\theta}](y) = \frac{(2\pi)^{3/2} i^n}{\sigma^3} \mathcal{F}_c^{-1}[h_{r,\nu}](y) Y_{n,0}(\theta), \qquad y \in [-1,1].$$

Applying Theorem 2.1 and the Cormack-type formula of (2.3), we find that

$$\begin{aligned} v(\sigma x\theta) &= \mathcal{R}^{-1}[w_{r,\sigma}](x) \\ &= \frac{Y_{n,0}(\theta)}{2\pi} \frac{d^2}{dx^2} \int_x^{+\infty} \frac{x P_n(y/x) w_n(y)}{y^2} dy, \qquad x \in (0,1], \end{aligned}$$

where

$$w_n(y) := \begin{cases} \frac{(2\pi)^{3/2} i^n}{\sigma^3} \mathcal{F}_c^{-1}[h_{r,\nu}](y), & \text{if } y \in (0,1], \\ 0, & \text{if } y > 1. \end{cases}$$

Substituting $s = \sigma x$, $t = \sigma y$, and recalling the definition of v, we derive formula (1.8). This completes the proof of Theorem 1.2.

3 Reconstructions via the FBP algorithms

Numerical reconstruction for Problem 1.1 with integer or half-integer $\nu \geqslant 0$ can be implemented as follows. As discussed in Section 1, we rely on *filtered back projection* (FBP) algorithms for inverting the Radon transform, unlike Theorem 1.1 and Theorem 1.2 which rely on Cormack-type inversion.

Step 1. Given the Hankel data h on $[0, r]$, set $h_{r,\nu}$ according formulas (1.7) and (1.9) as in Theorem 1.1 and Theorem 1.2. Define $g_{r,\theta}$ according to formulas (2.5) and (2.7):

$$g_{r,\theta}(x) = \begin{cases} \frac{2\pi i^{\nu}}{\sigma^2} h_{r,\nu}(x) e^{i\nu\varphi}, & \text{if } \nu \text{ is integer,} \\ \frac{(2\pi)^{3/2} i^n}{\sigma^3} h_{r,\nu}(x) Y_{n,0}(\theta), & \text{if } \nu \text{ is half-integer.} \end{cases}$$

Recall that $x \in [-1, 1]$ and $n = \nu - \frac{1}{2}$ for half-integer ν.

Step 2. Reconstruct v from $g_{r,\theta}$ according to the formulas of Theorem 2.1. For inverting $\mathcal{F}_c^{-1}$, we use its regularised version $\mathcal{F}_{m,c}^{-1}$ as in [15–17], which we recall below. For inverting the Radon transform, we use the FBP algorithms; see, for example, [10, 16, 17].

Step 3. Compute the result f on $[0, \sigma]$ as follows:

$$f(s) = \begin{cases} \frac{\sqrt{s}}{2\pi} \int_{-\pi}^{\pi} v(s\cos\phi, s\sin\phi) e^{-i\nu\phi} d\phi, & \text{if } \nu \text{ is integer,} \\ s \int_{\mathbb{S}^2} v(s\theta) Y_{n,0}(\theta) d\theta, & \text{if } \nu \text{ is half-integer.} \end{cases}$$

At Step 2, we approximate the operator $\mathcal{F}_c^{-1}$ in (1.5) by the finite rank operator $\mathcal{F}_{m,c}^{-1}$ defined by

$$\mathcal{F}_{m,c}^{-1}[g](y) := \sum_{j=0}^{m} \frac{1}{\mu_{j,c}} \psi_{j,c}(y) \int_{-1}^{1} \psi_{j,c}(x) g(x) dx. \tag{3.1}$$

The parameter m in (3.1) is the regularisation parameter; see [16, Section 2] for a discussion on its optimal choice.

Let $\tilde{\mathcal{H}}_{m,\nu}^{-1}[h]$ denote the result of our reconstruction described above from the Hankel data h with regularisation parameter m. We use the following measure of the quality of reconstruction f_{rec} of the preimage f:

$$\mathfrak{E}(f_{\mathrm{rec}}, h) := \frac{\|\mathcal{H}_{\nu}[f_{\mathrm{rec}}] - h\|_{\mathcal{L}^2([0,r])}}{\|h\|_{\mathcal{L}^2([0,r])}}. \tag{3.2}$$

In the numerical examples of the present work the choice of m based on *the residual minimisation principle* (that is, taking m minimising $\mathfrak{E}(\tilde{\mathcal{H}}_{m,\nu}^{-1}[h], h)$) is highly satisfactory:

it gives a stable reconstruction even from noisy data (without blow-ups in the configuration space) and leads to super-resolution for moderate levels of noise.

We present our examples in Section 3.1 and Section 3.2, where we always have $\sigma = 1$ and $c = r = 10$. Our numerical implementations rely on the values of the Hankel data h on the standard uniform grid with N points, where we take $N = 256$. In the examples with noise, the values of h at these points are altered by centered Gaussian white random noise independently of each other. All figures use the same legend:

- *dotted lines* represent the preimage f and its Hankel data h (possibly with noise);
- *bold lines* represent the PSWF-Radon reconstruction $\tilde{f} = \tilde{f}_m = \tilde{\mathcal{H}}_{m,\nu}^{-1}[h]$ and its Hankel transform with m chosen according to the residual minimisation principle (unless specified otherwise);
- *dashed lines* represent f_{naive} defined in (1.2) and its Hankel transform $\mathcal{H}_\nu[f_{\text{naive}}]$.

We focus on the cases when $\nu = 0$ and $\nu = 0.5$ as our reconstruction behave similarly for higher integer and half-integer orders. As mentioned in Section 1, this also illustrates reconstructions from band-limited Fourier transform under additional a priori assumption of spherical symmetry in dimensions $d = 2$ and $d = 3$; see Figure 1.1 and Figure 1.2.

3.1 Two step function

We start from a more detailed analysis of the example considered in Figure 1.1 and Figure 1.2, where f is the characteristic function of $[0.15, 0.3] \cup [0.5, 0.75]$. We study the resilience of the super-resolution demonstrated in these examples with respect to various levels of noise. In all our examples, one can see that selecting the regularisation parameter m according to the residual minimisation principle is adequate. In particular, we observe that the PSWF-Radon reconstruction $\tilde{f}_m$ with such m performs at least as well as f_{naive}, even for high levels of noise, while $\tilde{f}_m$ significantly outperforms f_{naive} for low levels of noise. In contrast to Figure 1.1 and Figure 1.2, we present our numerical results as 1D plots instead of 2D images, as this format is easier for comparisons.

3.1.1 Order $\nu = 0$

Here, we consider the PSWF-Radon reconstruction $\tilde{f}$ for $\nu = 0$ from its Hankel data given with three levels of white Gaussian noise: 0%, 20%, and 35%. Figure 3.3(a) is equivalent to Figure 1.1 and illustrates the reconstruction $\tilde{f}$ from noiseless data. Figure 3.3(b,c)

illustrate the reconstructions $\tilde{f}$ from noisy data: one can see that $\tilde{f}$ maintains super-resolution even for 20% noise (even though the location of the first step starts to shift), whilst $\tilde{f}$ resembles f_{naive} for 35% noise. The corresponding plots in the data space are given in Figure 3.4. Figure 3.5 illustrates the evolution of the residual plots of $\mathfrak{E}(\tilde{f}_m, h)$ defined in (3.2): as noise increases, the residual minimisation leads to smaller m and eventually the PSWF-Radon reconstruction $\tilde{f}$ loses its capability to super-resolution and becomes comparable to f_{naive}.

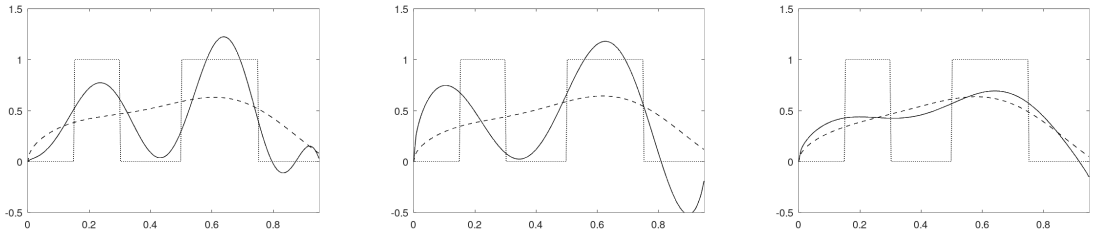

(a) **(b)** **(c)**

Figure 3.3: The PSWF-Radon reconstruction $\tilde{f}$ in comparison with f_{naive} and the preimage f for the order $\nu = 0$: (a) noiseless (b) 20% noise (c) 35% noise.

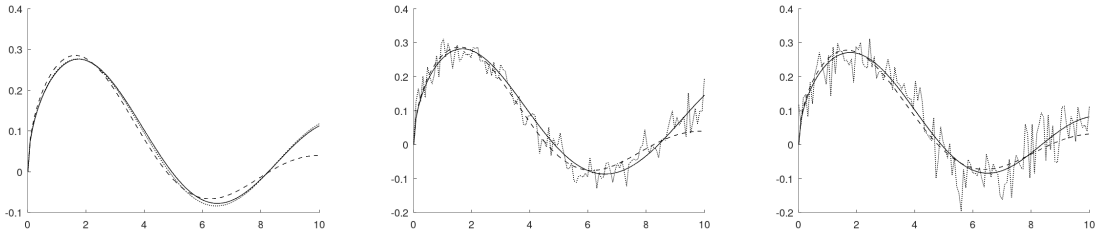

(a) **(b)** **(c)**

Figure 3.4: The Hankel transforms $\mathcal{H}_\nu[\tilde{f}]$ and $\mathcal{H}_\nu[f_{\text{naive}}]$ in comparison with the Hankel data h for the order $\nu = 0$: (a) noiseless, (b) 20% noise, (c) 35% noise.

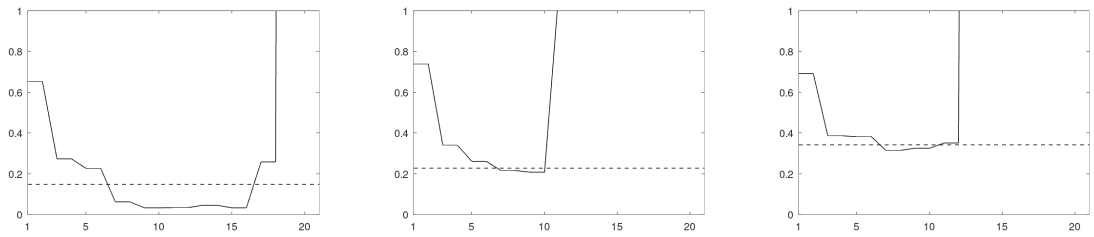

(a) **(b)** **(c)**

Figure 3.5: The dependence of the relative residual $\mathfrak{E}(\tilde{f}_m, h)$ on m in comparison with $\mathfrak{E}(f_{\text{naive}}, h)$ for the order $\nu = 0$: (a) noiseless, (b) 20% noise, (c) 35% noise.

3.1.2 Order $\nu = 0.5$

Here, we consider the PSWF-Radon reconstruction $\tilde{f}$ for $\nu = 0.5$ from its Hankel data given with three levels of white Gaussian noise: 0%, 5%, and 10%. Figure 3.6(a) is equivalent to Figure 1.2 and illustrates the reconstruction $\tilde{f}$ from noiseless data. Figure 3.6(b,c) illustrate the reconstructions $\tilde{f}$ from noisy data: one can see that $\tilde{f}$ maintains super-resolution for 5% noise (which is lower than for the case of $\nu = 0$), whilst $\tilde{f}$ resembles f_{naive} already for 10% noise. The corresponding plots in the data space are given in Figure 3.7. Figure 3.6 illustrates the evolution of the residual plots of $\mathfrak{E}(\tilde{f}_m, h)$ similarly to Figure 3.5.

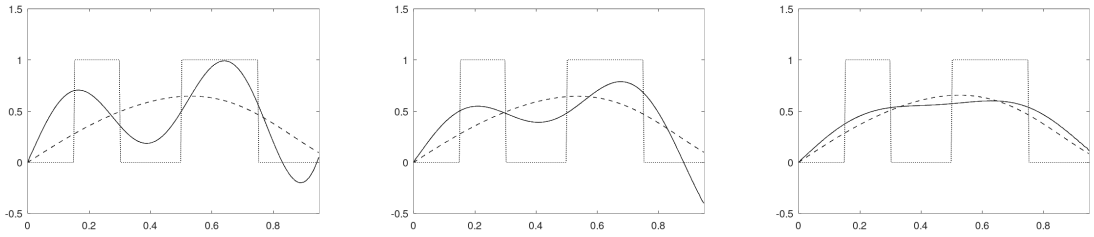

(a) **(b)** **(c)**

Figure 3.6: The PSWF-Radon reconstruction $\tilde{f}$ in comparison with f_{naive} and the preimage f for the order $\nu = 0.5$: (a) noiseless, (b) 5% noise, (c) 10% noise.

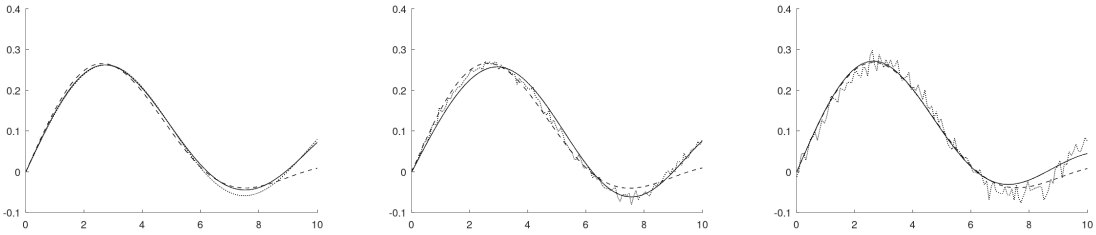

(a) **(b)** **(c)**

Figure 3.7: The Hankel transforms $\mathcal{H}_\nu[\tilde{f}]$ and $\mathcal{H}_\nu[f_{\text{naive}}]$ in comparison with the Hankel data h for the order $\nu = 0.5$: (a) noiseless, (b) 5% noise, (c) 10% noise.

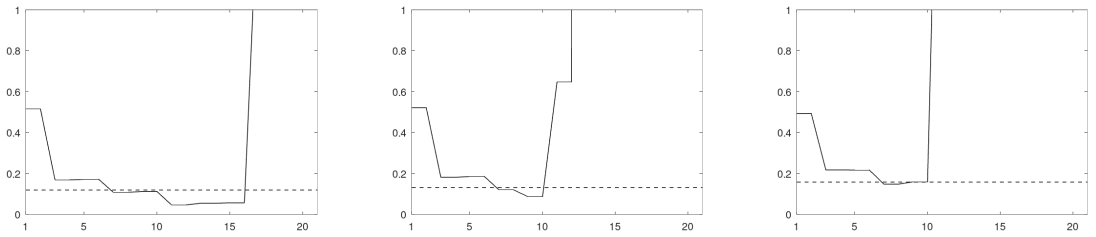

(a) **(b)** **(c)**

Figure 3.8: The dependence of the relative residual $\mathfrak{E}(\tilde{f}_m, h)$ on m in comparison with $\mathfrak{E}(f_{\text{naive}}, h)$ for the order $\nu = 0.5$: (a) noiseless, (b) 5% noise, (c) 10% noise.

3.2 Harmonics

Here, we consider $f = \sin(\omega s)$ truncated to the interval $s \in [0, \sigma]$, where $\sigma = 1$, from its Hankel data limited to $[0, r]$, where $r = 10$. This example is inherently difficult for Problem 1.1 as the Hankel data on $[0, r]$ rapidly decays shortly after ω exceeds r (that is, it becomes an insignificant part of the full Hankel transform). In particular, f_{naive} fails to reconstruct f adequately for such ω. We examine the extent to which the PSWF-Radon reconstruction $\tilde{f}$ can overcome this limit for the orders $\nu = 0$ and $\nu = 0.5$ at various levels of noise.

3.2.1 Order $\nu = 0$

Figure 3.9 shows the evolution with respect to ω of the reconstructions $\tilde{f}$ and f_{naive} for the case of 20% white Gaussian noise and $\nu = 0$. Figure 3.9(a) illustrates that f_{naive} has already deteriorated significantly from f at frequency $\omega = 11.32$, whereas $\tilde{f}$ is fairly

accurate. Figure 3.9(b) shows that $\tilde{f}$ starts to deteriorate from f around $\omega = 13.68$, whereas f_{naive} essentially reduces to 0. Figure 3.9(c) illustrates the behaviour of these reconstructions at higher frequencies. Thus, for this level of noise, the PSWF-Radon approach extends the range of frequencies by around 20% in comparison with f_{naive}.

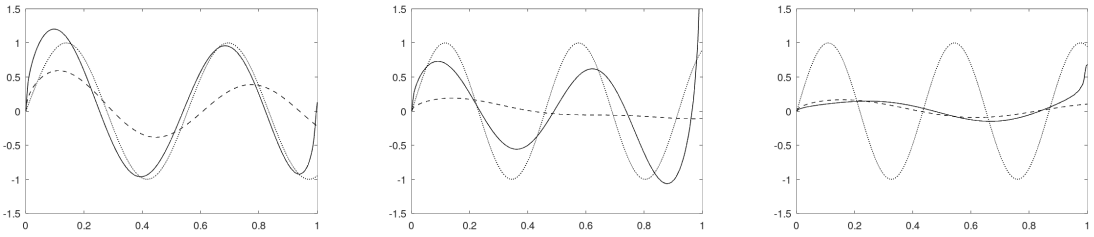

(a) **(b)** **(c)**

Figure 3.9: The PSWF-Radon reconstruction $\tilde{f}$ in comparison with f_{naive} and the preimage $f = \sin(\omega x)$ for the order $\nu = 0$ and the Hankel data with 20% noise: (a) $\omega = 11.32$, (b) $\omega = 13.68$, (c) $\omega = 14.47$.

In turn, for the noiseless case, we succeeded to extend the range of frequencies by around 50% in comparison with f_{naive}. Figure 3.10 shows the evolution with respect to ω of the PSWF-Radon reconstruction $\tilde{f}$ for the noiseless case beyond the frequencies considered in Figure 3.9. Note that f_{naive} remains essentially 0 for such high frequencies. Figure 3.10(a,b) shows that $\tilde{f}$ is fairy accurate for frequencies up to around 17. Figure 3.10(c) shows that, in practice, the PSWF-Radon approach is limited by the precision of numerical computations, despite its theoretical capability to handle arbitrary frequencies.

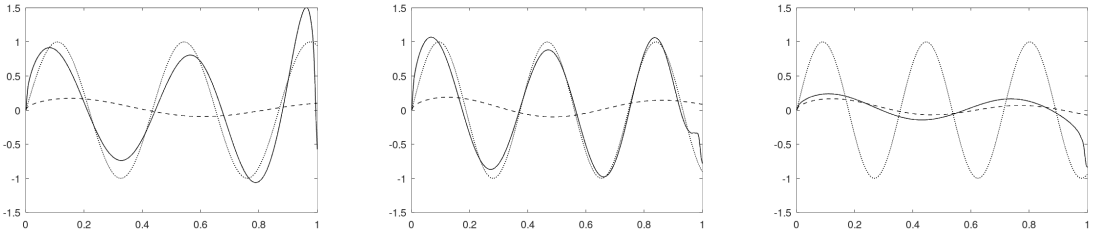

(a) **(b)** **(c)**

Figure 3.10: The PSWF-Radon reconstruction $\tilde{f}$ in comparison with f_{naive} and the preimage $f = \sin(\omega x)$ for the order $\nu = 0$ and noiseless Hankel data: (a) $\omega = 14.47$, (b) $\omega = 16.84$, (c) $\omega = 17.63$.

3.2.2 Order $\nu = 0.5$

Figure 3.11 shows the evolution with respect to ω of the reconstructions $\tilde{f}$ and f_{naive} for the case of 5% white Gaussian noise and $\nu = 0.5$. Figure 3.11(a) illustrates that f_{naive} has already deteriorated significantly from f at frequency $\omega = 10.53$, whereas $\tilde{f}$ is fairly accurate. Figure 3.11(b) shows that $\tilde{f}$ starts to deteriorate from f around $\omega = 11.32$, whereas f_{naive} essentially reduces to 0. Figure 3.11(c) illustrates the behaviour of these reconstructions at higher frequencies. Thus, for this level of noise, the PSWF-Radon approach extends the range of frequencies by around 7.5% in comparison with f_{naive}.

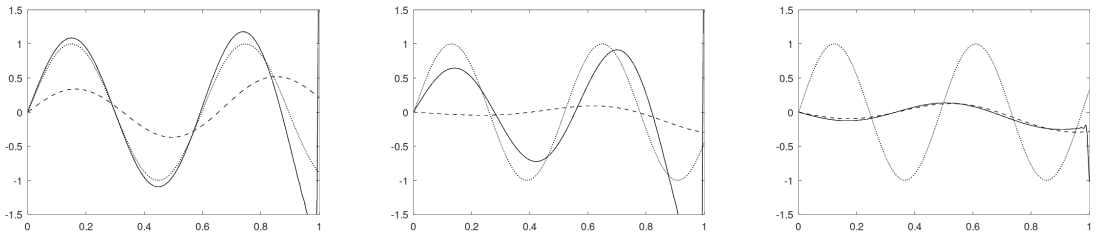

(a) **(b)** **(c)**

Figure 3.11: The PSWF-Radon reconstruction $\tilde{f}$ in comparison with f_{naive} and the preimage $f = \sin(\omega x)$ for the order $\nu = 0.5$ and the Hankel data with 5% noise: (a) $\omega = 10.53$, (b) $\omega = 11.32$, (c) $\omega = 12.11$.

In turn, for the noiseless case, we succeeded to extend the range of frequencies by around 40% in comparison with f_{naive}. Figure 3.12 shows the evolution with respect to ω of the PSWF-Radon reconstruction $\tilde{f}$ for the noiseless case beyond the frequencies considered in Figure 3.11. Note that f_{naive} remains essentially 0 for such high frequencies. Figure 3.12(a,b) shows that $\tilde{f}$ is fairy accurate for frequencies up to around 15. Figure 3.12(c) illustrates the same conclusion as for Figure 3.10(c).

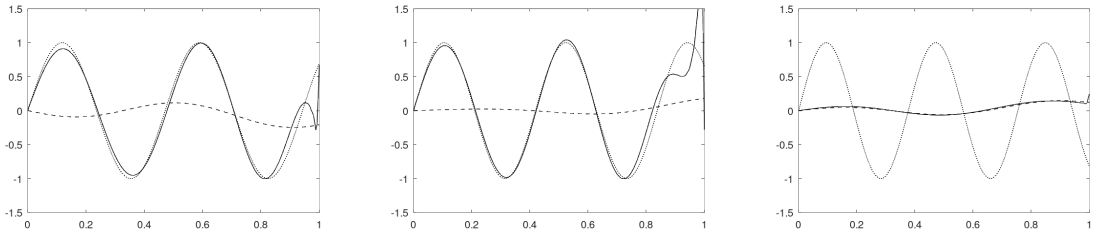

(a) **(b)** **(c)**

Figure 3.12: The PSWF-Radon reconstruction $\tilde{f}$ in comparison with f_{naive} and the preimage $f = \sin(\omega x)$ for the order $\nu = 0.5$ and noiseless Hankel data: (a) $\omega = 13.33$, (b) $\omega = 15$, (c) $\omega = 16.67$.

From the figures presented in Section 3.2, one can see that, in the case of noiseless data, the PSWF-Radon reconstructions $\tilde{f}$ for $\nu = 0$ and $\nu = 0.5$ have similar super-resolution capability. However, the performance of $\tilde{f}$ for $\nu = 0$ is notably superior in the presence of noise.

3.3 Implementation details

We follow Steps 1-3 formulated at the beginning of Section 3.

In our examples for Problem 1.1, the Hankel data h is given on the uniform grid with 256 points on interval $[0, r]$, with $r = 10$. We reconstruct unknown function f on uniform grid with 256 points on $[0, \sigma]$, where $\sigma = 1$. To generate data and also compute the residuals in the data space, we evaluate integral of (1.1) using the trapezoidal rule.

Our numerical implementation of operator $\mathcal{F}_{m,c}^{-1}$ defined in (3.1) relies on the Spheroidal Library of [1], which is available at `https://github.com/radelman/scattering`. Unfortunately, eigenvalues of the PSWFs are not available in this library, so we computed them using the approach of [12, Section 4.1]. It is important to note that the computations of the eigenvalues and the integrals in (3.1) require oversampling due to high oscillations of PSWFs. Using linear interpolation for the Hankel data, we get samples on the uniform grid with 1024 points.

In dimension $d = 2$, which corresponds to integer ν, we use the Fourier-based implementation of filtered back projection (FBP) algorithm for the Radon transform inversion from NFFT3 library; see survey [19]. In dimension $d = 3$, which corresponds to half-integer ν, we also use this library for reconstructions from the integrals over planes. Note that this version of the FBP algorithm is significantly less common so we relied on the

numerical implementations from [10].

Note that at Step 2, for fixed m, only one inversion by $\mathcal{F}_{m,c}^{-1}$ is sufficient in view of separation of radial and angle variables x and θ, respectively. Therefore, the overall memory and time complexity of the algorithm is dominated by the Radon inversion. For fixed $\nu \in \mathbb{N}$, reconstruction was performed on a personal laptop (AMD Ryzen 7 7840U) using 16 threads and required less than 1 second (for grid sizes up to 512) with negligible memory usage. For $\nu \in \frac{1}{2} + \mathbb{N}$, reconstruction required nearly 2 minutes on workstation (AMD 3995W) with 64 threads and 60GB of RAM. Such difference of required resources is due to dimensionality of the corresponding Radon inversion – 2D and 3D for integer and half-integer ν, respectively.

In our experiments, we also observed the Gibbs phenomenon at the boundary point $x = \sigma = 1$ for reconstruction $\tilde{f}$, see, for example, Figure 3.11(c) and Figure 3.12. We explain this phenomenon by a combination of the following factors:

- harmonic phantoms in Figures 3.11, 3.12 do not vanish at the boundary point $s = 1$;
- function $w_{r,\sigma}$ in Theorem 2.1 reconstructed for fixed m using $\mathcal{F}_{m,c}^{-1}$ does not necessarily belong to the range of the Radon transform on functions supported in B_1;
- our implementation of Radon inversion strongly relies on the assumption of compactly supported input (we use *zero padding* of the input to increase precision of the corresponding Fourier integration).

In particular, recall that the Radon transform $w_{r,\sigma}(x, \theta)$ of a function supported in the ball B_1 vanishes as $|x| \to 1$ at a specific rate (see [25, Theorem 1.6]). To decrease the ripple at the boundary, one may increase σ so that considered $f = f(s)$ in Problem 1.1 vanishes near the boundary point $s = \sigma$ or/and apply a smooth cut-off for $w_{r,\sigma}(x, \theta)$ near the boundary $|x| = 1$. However, we did not pursue this task as auxiliary regularisation might affect the investigated stability.

The source code of our algorithms based on the PSWF-Radon approach generating the presented data can be found at `https://github.com/fedor-goncharov/pswf-radon`.

4 Concluding remarks

Note that Problem 1.1 is equivalent to the inversion of the band-limited Hankel transform $\mathcal{H}_{\nu,c}$ with $c = r\sigma$ defined by

$$\mathcal{H}_{\nu,c}[f](x) := \int_0^1 f(y) J_\nu(cxy)\sqrt{cxy}\, dy, \qquad x \in [0,1].$$

The operator $\mathcal{H}_{\nu,c}$ is well-studied in the literature and its properties are similar in many respects to the band-limited Fourier operator $\mathcal{F}_c$; see, for example, [20, 32]. One can approach Problem 1.1 using the singular value decomposition for the operator $\mathcal{H}_{\nu,c}$. Compared to this approach, the main advantages of the present work based on the PSWF-Radon approach of [15–17] are summarised below.

- Theorem 1.1 and Theorem 1.2 involve classical functions only, namely, the Chebyshev and Legendre polynomials and the prolate spheroidal wave functions of [26,31].
- In particular, our formulas require the same set of eigenfunctions $(\psi_{j,c})_{j\in\mathbb{N}}$ for different ν, that is, classical PSWFs, unlike the approach based on the eigenfunctions of $\mathcal{H}_{\nu,c}$. This is particularly convenient for problems involving simultaneous inversion of $\mathcal{H}_{\nu,c}$ for many ν.
- We proceed from efficient numerical implementation for band-limited Fourier inversion in multidimensions developed in [16,17] that achieves super-resolution even for noisy data. We observe similar numerical properties for Problem 1.1.

Next, we remark that our work gives the first numerical illustration of the PSWF-Radon approach for band-limited Fourier inversion in three dimensions; see Figure 1.2 and Section 3.1.2. However, further numerical investigations are required for reconstructions without a-priori assumption of spherical (or spherical-type) symmetry. An important challenge for the PSWF-Radon approach is that the observed resilience of our reconstructions to the noise is significantly lower in the case of $d = 3$ compared to $d = 2$. Further natural challenges also include reduction of computational costs for PSWF-Radon reconstructions from band-limited Hankel data.

Furthermore, various a-priori assumptions on unknown function f in Problem 1.1 can enhance super-resolution properties. Possible approaches to this (and similar improvements for band-limited Fourier inversion for $d = 2$ and $d = 3$) include combinations of the PSWF-Radon approach [15–17] with the methods of [3, 24] based on generalised PSWFs, and, for further enhancement, variational and iterative methods including machine learning techniques; see, for example, [2, 23, 30] and references therein.

5 Acknowledgements

The work was initiated in the framework of the internship of R. Zaytsev at the Centre de Mathématique Appliquées of Ecole Polytechnique under the supervision of R.G. Novikov in June-August 2023.

References

[1] R. Adelman, N.A. Gumerov, R. Duraiswami, Software for computing the spheroidal wave functions using arbitrary precision arithmetic, (2014), CoRR abs/1408.0074, arXiv:1408.0074.

[2] N. Alibaud, P. Maréchal, Y. Saesor, A variational approach to the inversion of truncated Fourier operators. *Inverse Problems*, **25**(4) (2009), 045002.

[3] L. Audibert, S. Meng, Shape and parameter identification by the linear sampling method for a restricted Fourier integral operator, *Inverse Problems*, **40**(9) (2024).

[4] G. Beylkin, L. Monzón, Nonlinear inversion of a band-limited Fourier transform, *Applied and Computational Harmonic Analysis*, **27**(3) (2009), 351–366.

[5] A. Bonami, A. Karoui, Uniform bounds of prolate spheroidal wave functions and eigenvalues decay, *Comptes Rendus de l'Académie des Sciences, Series I*, **352**(3) (2014), 229–234.

[6] A. Bonami, A. Karoui, Spectral decay of time and frequency limiting operator, *Applied and Computational Harmonic Analysis* **42**(1) (2017), 1–20.

[7] E. J. Candès, C. Fernandez-Granda, Towards a mathematical theory of super-resolution, *Communications on Pure and Applied Mathematics*, **67** (2014), 906–956.

[8] A.M. Cormack, Representation of a function by its line integrals, with some radiological applications. *Journal of Applied Physics* **34**(9) (1963), 2722–2727.

[9] R.W. Gerchberg, Superresolution through error energy reduction, *Optica Acta: International Journal of Optics*, **21**(9) (1974), 709–720.

[10] F. Goncharov, A geometric based preprocessing for weighted ray transforms with applications in SPECT, *Journal of Inverse and Ill-posed Problems* **29** (3) (2021), 435–457.

[11] H.A. Hasanov, V.G. Romanov, *Introduction to inverse problems for differential equations*. Second edition, Springer (2021), 515 pp.

[12] X. Hong, V. Rokhlin, N. Yarvin. Prolate spheroidal wavefunctions, quadrature and interpolation. *Inverse problems* **17** (2001), 805.

[13] M. Isaev, R.G. Novikov, Hölder-logarithmic stability in Fourier synthesis, *Inverse Problems* **36**(12) (2020), 125003.

[14] M. Isaev, R.G. Novikov, Stability estimates for reconstruction from the Fourier transform on the ball, *Journal of Inverse and Ill-posed Problems*, **29**(3) (2021), 421–433.

[15] M. Isaev, R.G. Novikov Reconstruction from the Fourier transform on the ball via prolate spheroidal wave functions, *Journal de Mathématiques Pures et Appliquées*, **163** (2022), 318–333.

[16] M. Isaev, R.G. Novikov, G.V. Sabinin, Numerical reconstruction from the Fourier transform on the ball using prolate spheroidal wave functions, *Inverse Problems*, **38**(10) (2022), 105002.

[17] M. Isaev, R.G. Novikov, G.V. Sabinin, Super-resolution reconstruction from truncated Fourier transform, *Extended abstracts MWCAPDE*, 2023, Birkhäuser, DOI: 10.1007/978-3-031-41665-1_7.

[18] S. Karnik, J. Romberg, M. A. Davenport, Improved bounds for the eigenvalues of prolate spheroidal wave functions and discrete prolate spheroidal sequences. *Applied and Computational Harmonic Analysis* **55**(1) (2021), 97–128.

[19] J. Keiner, S. Kunis, D. Potts. Using NFFT 3—a software library for various nonequispaced fast Fourier transforms. *ACM Transactions on Mathematical Software (TOMS)*, **36**(4) (2009), 1–30.

[20] A. Karoui, T. Moumni, Spectral analysis of the finite Hankel transform and circular prolate spheroidal wave functions, *Journal of Computational and Applied Mathematics* **233**(2) (2009), 315–333.

[21] M.I. Kolobov, V.N. Beskrovnyy, Quantum theory of super-resolution for optical with circular apertures, *Optics Commun.* **264** (2006), 9–12.

[22] A. Lannes, S. Roques, M.-J. Casanove, Stabilized reconstruction in signal and image processing: I. partial deconvolution and spectral extrapolation with limited field. *Journal of Modern Optics*, **34**(2) (1987), 161–226.

[23] A. Laghrib, F. Zahra Ait Bella, M. Nachaoui, F. Jauberteau, Bilevel optimal parameter learning for a high-order nonlocal multiframe super-resolution problem, *Inverse Problems* **40** (1) (2023) 015004.

[24] S. Meng, Data-driven Basis for Reconstructing the Contrast in Inverse Scattering: Picard Criterion, Regularity, Regularization, and Stability, *SIAM J. Appl. Math.*, **83**(5) (2023), 2003–2026.

[25] F. Natterer, The Mathematics of Computerized Tomography. *Society for Industrial Mathematics*, (2001), 184 pp.

[26] C. Niven, On the conduction of heat in ellipsoids of revolution, *Philosophical transactions of the Royal Society of London*, **171**(1880) 117–151.

[27] R.G. Novikov, B. L. Sharma, Inverse source problem for discrete Helmholtz equation, *Inverse Problems* **40**(10) (2024), 105005.

[28] A. Papoulis, A new algorithm in spectral analysis and band-limited extrapolation. *IEEE Transactions on Circuits and Systems*, **22**(9) (1975), 735–742.

[29] A. Puro, Cormack-type inversion of exponential Radon trans-form. *Inverse problems*, **17**(1) (2001), 179.

[30] O. Scherzer, B. Hofmann, Z. Nashed, Gauss–Newton method for solving linear inverse problems with neural network coders. *Sampl. Theory Signal Process. Data Anal.* **21** (2023), 25.

[31] D. Slepian, H.O. Pollak, Prolate spheroidal wave functions, Fourier analysis and uncertainty — I, *Bell System Technical Journal*, **40** (1) (1961), 43–63.

[32] D. Slepian, Prolate spheroidal wave functions, Fourier analysis and uncertainty–IV: Extensions to many dimensions; generalized prolate spheroidal functions, *Bell System Technical Journal*, **40** (1964), 3009–3057.

[33] A.N. Tikhonov, V. Y. Arsenin, *Solutions of ill-posed problems.* Washington : New York : Winston ; distributed solely by Halsted Press, (1977), 258 p.

[34] L. L. Wang, Analysis of spectral approximations using prolate spheroidal wave functions. *Mathematics of Computation* **79** (2010), no. 270, 807–827.

[35] H. Xiao, V. Rokhlin, N. Yarvin, Prolate spheroidal wavefunctions, quadrature and interpolation. *Inverse Problems* **17**(4) (2001), 805–838.